

Abstracts

# Radiological Technology



# Evaluation of radiation dose to infants in CT and other x-ray diagnostic radiology

Naruto Sugimoto, Takahiko Aoyama, Shuji Koyama, Chiyo Yamauchi-Kawaura

Department of Radiological Sciences, Graduate School of Medicine, Nagoya University, Nagoya, Japan

## Introduction

Recent technical innovation of diagnostic radiology conducted worldwide increase in the frequency of x-ray examinations, in particular of CT examinations, not only for adults but also for pediatric patients. Since the risk inducing cancer for infants has been estimated to be factors of 3-4 higher compared with that for adults (see Fig. 1 [1]), evaluation of exposure doses to infants would be important.

Although we extensively evaluated the doses for adults and for 6-years-old children [2,3], dose levels in CT and other x-ray diagnostic radiology for infants have not been investigated. In the present study, we examined organ and effective doses to newborn patients who underwent CT and other x-ray diagnostic radiology, based on in-phantom dose measurements, and compared the doses with those for adult patients.

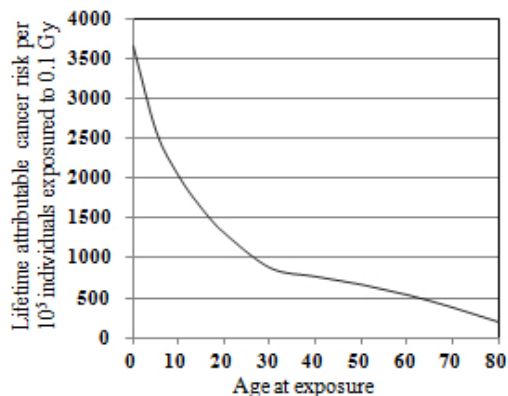


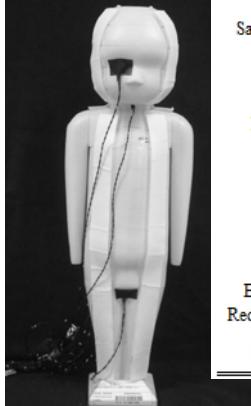
**Fig. 1** Lifetime attributable risk of cancer incidence per  $10^5$  individuals exposed to 0.1 Gy as a function of age at exposure [1].

## Materials and Methods

### 1. In-phantom dosimetry system

Dose measurements were performed with a newborn anthropomorphic phantom, ATOM 703 (CIRS, Norfolk, VA), the scheme of which is shown in Fig. 2. The phantom represented a standard newborn baby, 3.5 kg in weight and 51 cm tall. Photodiode x-ray sensors were installed at the positions of various tissues and organs defined in the International Commission on Radiological Protection (ICRP) Publication 103 [4] to evaluate the effective dose, excepting lens. These positions and the number of photodiode sensors implanted in each tissue or organ are shown in Fig. 2. Radiation doses for small tissues and organs such as the thyroid and the bladder were measured with a sin-

gle sensor, and doses for large organs such as the brain and the colon were measured with several sensors.



Tissue or organ	Number of sensors	$w_t$
Brain	2	0.01
Lens	1	-
Salivary glands	1	0.01
Thyroid	1	0.04
Lung	1	0.12
Breast	1	0.12
Esophagus	2	0.04
Liver	1	0.04
Stomach	1	0.12
Colon	4	0.12
Ovary	1	0.08
Bladder	1	0.04
Testis	1	0.08
Bone surface	11	0.01
Red bone marrow	10	0.12
Skin	2	0.01
Remainder	9	0.12

**Fig. 2** The newborn phantom (CIRS, Norfolk, VA) used. Also shown are the numbers of photodiode sensors implanted in each position of tissues and organs and tissue weighting factors  $w_t$  listed in ICRP 103.

X-ray sensors used for the in-phantom dosimetry system were planer-type of silicon pin-photodiodes, Hamamatsu S8385-04, which were small sized but highly sensitive for diagnostic x rays. Since the sensitivity of a single photodiode of this type differed by the incidence direction of x-rays between front and back, two photodiodes were glued together back to back with epoxy cement, and were used as a single sensor with parallel connection. The sensor was wrapped up with 11  $\mu\text{m}$ -thick aluminum foil for electromagnetic shielding and connected to a pair of twisted carbon-fiber cables, which were tissue equivalent.

Signal current generated by x-ray incidence on a photodiode sensor was fed through the cables to a current integrator, and integrated to the total charge proportional to the dose absorbed by the photodiode sensor. Dose calibration of the photodiode dosimeters was performed against a Radcal 9015 with a  $6\text{ cm}^3$  ion chamber. The values of exposure dose in the unit of coulomb per kilogram obtained with the ion chamber were converted to the values of absorbed dose for soft tissue by using the ratio of mass energy absorption coefficient of soft tissue to that of air at the effective energy of x rays used. Output signals from photodiode dosimeters were read out on a personal computer, from which organ and effective doses were computed according to guidelines published in ICRP Pub.103 [4].

## 2. Dose measurements

Patient exposure dose in diagnostic radiography were measured for the typical examinations of head, chest, abdomen and hip-joint using various types of x-ray generators. All of the measurements were performed with patient-size dependent imaging protocols.

Doses in CT examinations were evaluated with four 64- and 16-detector row CT scanners from worldwide manufacturers, *i.e.* General Electric, Philips, Toshiba and Siemens. All of these scanners were operated with patient-size-dependent imaging protocols with and without automatic tube current modulation (ATCM). Dose measurements were performed with technical parameters clinically used in plain or non-contrast head CT, chest and cardiac CT, and abdomen including pelvis and abdomen with bolus tracking CT scans.

## Results and Discussion

Figure 3(a) shows organ doses in head CT scans for newborn patients obtained with a 64-detector row CT scanner from Toshiba. Brain and lens doses, *i.e.* the doses for organs within the scan region, of 40 and 38 mGy were relatively high, though they were approximately 1 – 2 times lower than the doses of 42 – 71 mGy and 45 – 88 mGy observed for adult patients. On the other hand, though red-bone-marrow dose of 12 mGy was relatively low, it was approximately 2 – 4 times higher than that of 3 – 6 mGy for adults. The reason of which would mainly be due to a large weight-percentage of red bone marrow at the cranium for newborn babies than that for adults, *e.g.* 3 times larger weight-percentage for newborns than for adults.

Shown in Fig. 3(b) are organ doses in chest and heart CT scans for newborn patients obtained with the 64-detector row CT scanner from Toshiba. The doses for organs within the scan region as thyroid, lung, breast, heart, esophagus and liver, of 8 – 10 mGy in chest CT were approximately 2 – 4 times lower than those of 20 – 32 mGy for adults observed with the same scanner. On the other hand, doses for such organs located close to the scan region as colon and salivary gland were approximately 2 – 3 times higher for newborns than for adults because of small separations of these organs from the scan region for newborns.

Figure 3(c) shows organ doses in two types of abdominal CT scans for newborn patients obtained also with the 64-detector row CT scanner from Toshiba. Organ doses for organs within the scan region as liver, stomach, colon, ovary and bladder, of 12 mGy in abdomen including pelvis CT scans were approximately 2 – 3 times lower than those of 27 – 33 mGy in adult abdominopelvic CT scans observed with the same scanner. On the other hand, dose of 10 mGy for breast located close to the scan region was only 1.8 times lower than that for adults of 18 mGy.

Organ doses for newborn patients obtained with the Toshiba scanner were similar to those observed with

other CT scanners.

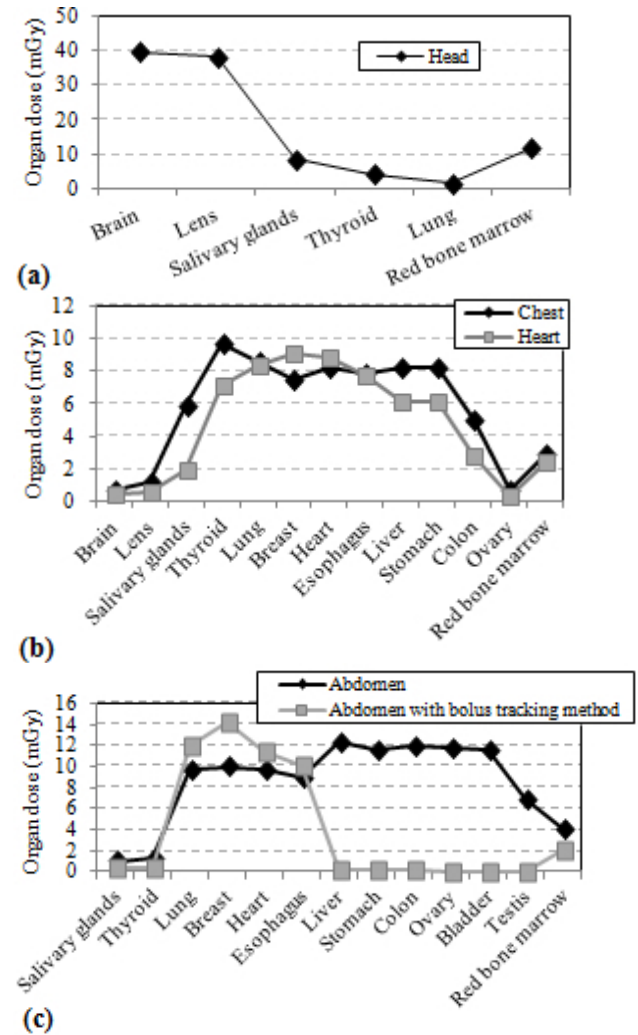


**Fig. 3** Organ doses in (a) head, (b) chest, heart and (c) two types of abdominal CT scans for newborn patients obtained with a 64-detector row CT scanner from Toshiba.

## Reference

- [1]National Research Council of the National Academies, "Health risks from exposure to low levels of ionizing radiation," BEIR VII phase 2 (2006).
- [2]C. Yamauchi-Kawaura et al., "Radiation dose evaluation in multidetector-row CT imaging for acute stroke with an anthropomorphic phantom," *Br. J. Radiol.* **83**, 1029-1041 (2010).
- [3]K. Fujii et al., "Radiation dose evaluation in 64-slice CT examinations with adult and paediatric anthropomorphic phantoms," *Br. J. Radiol.* **82**, 1010-1018 (2009).
- [4]International Commission on Radiological Protection, "P103: The 2007 Recommendations of the International Commission on Radiological Protection," *Ann. ICRP* **37** (2007).

## Author address

E-Mail: [sugimoto.naruto@h.mbox.nagoya-u.ac.jp](mailto:sugimoto.naruto@h.mbox.nagoya-u.ac.jp)

# ENERGY ESTIMATION IN A PHANTOM IN X-RAY CT : ANALYSIS USING MONTE CARLO METHOD

Shimpei Kondo<sup>1)</sup>, Shuji Koyama<sup>1)</sup>

1) Department of Radiological Sciences, Nagoya University Graduate School of Medicine, Nagoya, Japan

## Introduction

X-ray entered into a phantom is absorbed and scattered. In-phantom x-ray spectrum has the potential to differ from incident x-ray spectrum when continuous x-ray enters into object. We have small semiconductor dosimeters, which are very useful to measure doses in phantom. The semiconductor dosimeters have large energy dependence and, output values of them are influenced by changes in beam quality. It is important to measure x-ray energy spectrum and effective energy in phantom to know appropriate calibration factor, because calibration factor for the semiconductor dosimeters is required to estimate correct absorbed dose. It is, however, practically difficult to measure x-ray energy spectrum or half-value-layer in phantom. In this study, in-phantom x-ray energy spectrum and effective energy were analyzed by using Monte Carlo simulation which had the advantage of being able to calculate energy spectrum in difficult measurement situation.

## Materials and Methods

X-ray energy spectrum and effective energy in a phantom undergoing x-ray CT scan were analyzed by Electron Gamma Shower 5 (EGS5) Monte Carlo simulation code.

### 1. Monte Carlo Simulation Geometry

X-ray-focus isocenter distance was 60 cm. The cylindrical phantom consisted of water, 32 cm in diameter and 20 cm in length. Twenty five small water discs of 1 cm diameter were put inside the phantom, along horizontal and vertical axis of an axial plane at 0.2 cm intervals. Locations of each of four small discs nearest the phantom surface were placed at 0.7, 1.0, 1.3, and 1.6 cm from the phantom surface. **Fig.1** shows geometry of this calculation and the cylindrical water phantom.

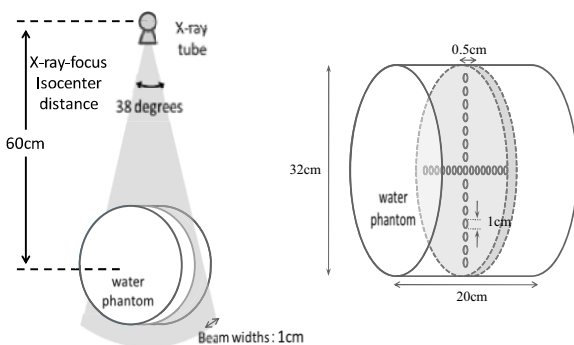


**Fig.1** Geometry of this simulation undergoing x-ray CT and cylindrical water phantom

### 2. Beam-shaping filter incorporated in simulation

X-ray CT is generally equipped with beam-shaping filter in front of the x-ray tube radiation window. By the beam-shaping filter, incident x-ray emitted from the target is adjusted to certain energy at CT detector after passing through phantom.

Before incident to the phantom, therefore, dose distribution and beam quality of x-rays originally emitted from the target are changed by the beam-shaping filter. For making x-ray CT simulation more concrete, the effect of beam-shaping filter that is contributed to x-ray attenuation and beam hardening, must be incorporated in incident fan beam. **Fig.2** shows effective energy and dose distribution based on measurement data from x-ray CT (TCT-300; Toshiba Medical, Tochigi, Japan), which were incorporated in incident fan beam of our simulation code.

To take into account the effect of beam-shaping filter, incident fan beam was divided into 7 parts (0-4, 4-5, 5-6, 6-7, 7-8, 8-9, and 9-18 degrees) on the half side of the fan beam and seven different spectrums were used in each part. Effective energy of the energy spectrums were 54, 57, 59, 62, 64, 72, and 73 keV from the center part to the outer part, respectively, and the number of photon corresponding to dose distribution data was used in each degree (0-18 degrees) of fan beam.

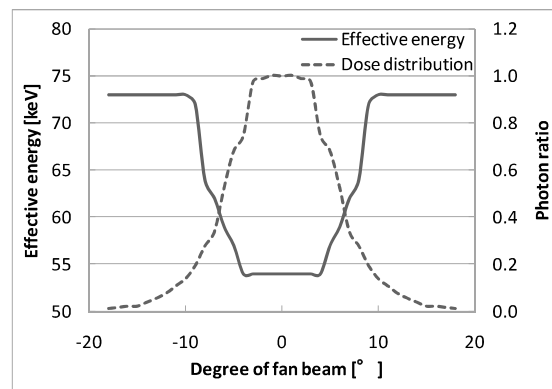


**Fig.2** Effective energy and dose distribution data incorporated in this simulation

### 3. Obtaining in-phantom spectrum and effective energy

The photons passing through the small disc inside the phantom were counted with respect to each energy bin, and those were used for calculating in-phantom energy spectrum and effective energy along x axis and y axis of an axial plane of the phantom. The total number of photon source was  $1.44 \times 10^9$ .

## Results and Discussions

**Fig.3** shows two in-phantom x-ray spectrums with the lowest and highest effective energy (55.92 keV and 56.28 keV) and incident spectrum (effective energy:  $E_{eff} = 54$  keV).

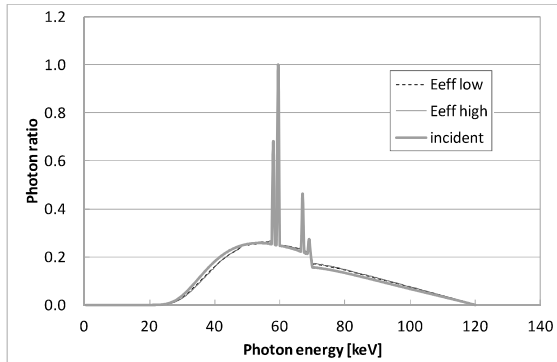


**Fig.3** Comparison of in-phantom x-ray spectrum with incident x-ray spectrum.

Change of effective energy in the phantom is shown in **Fig.4**. The in-phantom effective energy is 55.92 keV at the depth of 1 cm (raised by 3.61 % compared to effective energy of the incident x-rays), and 55.97 keV at the depth of 16 cm (raised by 3.65 %). The spread between the lowest and highest in-phantom effective energy is less than 1 keV.

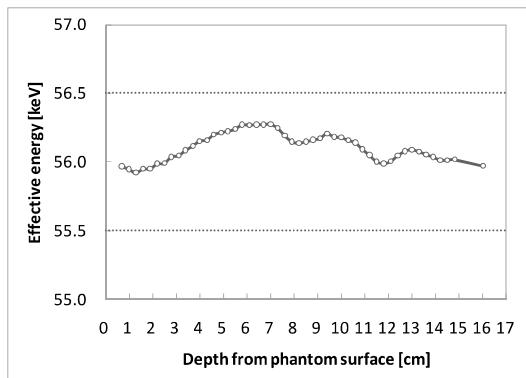


**Fig.4** Change of in-phantom effective energy in each depth from the phantom surface

One would think that continuous x-ray entered in phantom is absorbed, and beam quality becomes just harder. That is true in looking at only primary x-ray, but not true with the scattered x-ray. In this research, little difference existed between incident and in-phantom effective energy. In the phantom, effective energy in each depth from the phantom surface also had little difference. At the point of each depth, low energy component of the x-ray spectrum was reduced by beam hardening effect. In contrast, low energy x-rays generated in another area by Compton scattering were absorbed to the point, and they were contributed to low energy component of the spectrum. The proportion between beam hardening and Compton scattering is important component of changing process of effective energy. Thus, in-phantom beam quality which contains scattered x-ray is not just harder.

**Fig.5** shows the energy dependence of small semiconductor dosimeter owned Nagoya University. The difference of sensitivity of semiconductor dosimeter between incident and in-phantom effective energy is shown in **Table 1**. Relatively small changing of effective energy in phantom had little effect on calibration factor for the semi-conductor dosimeter.

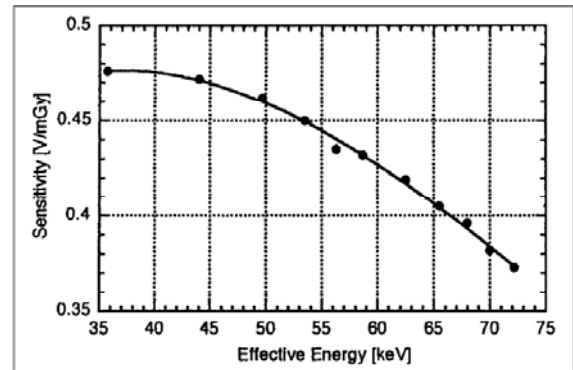


**Fig.5** Energy dependence of small semiconductor dosimeter (made by T Aoyama; Nagoya University 2002) [1].

**Table 1** Difference of sensitivity of small semiconductor dosimeter for effective energy

	Effective energy	Sensitivity	Difference for incident $E_{eff}$	
	[keV]	[V/mGy]	[V/mGy]	[%]
incident	54.00	0.448	-	-
in-phantom	55.92(low)	0.440	-0.008	-1.79
	56.28(high)	0.441	-0.007	-1.56

## Conclusions

In-phantom x-ray spectrum and effective energy were analyzed by using Monte Carlo simulation (EGS5). Little difference exists between incident and in-phantom effective energy.

## References

- [1] T. Aoyama, S. Koyama, C. Kawaura, :An in-phantom dosimetry system using pin silicon photodiode radiation sensors for measuring organ doses in x-ray CT and other diagnostic radiology, Med. Phys. 29, 1504-1510, 2002
- [2] M.Tucker, G. Barnes, D. Chakraborty :Semiempirical model for generating tungsten target x-ray spectra, Med. Phys.18, 211-218, 1991

## Author address

E-Mail: kondo.shimpei@e.mbox.nagoya-u.ac.jp

# APPLICATION OF THE NEW CT TECHNIQUE USING THE MONTE CARLO SIMULATION

Daiki Hayashi<sup>1)</sup>, Shuji Koyama<sup>1)</sup>

1) Department of Radiological Sciences, Nagoya University Graduate School of Medicine, Nagoya, Japan

## Introduction

Recent years, tremendous advances in computed tomography (CT) scan technology and applications have been increased in clinical utilization. Among them, we focused on dual energy CT (DECT) and CT-auto exposure control (CT-AEC). In DECT, computed tomography dose index (CTDI) for DECT is measured using same method as the measurement method of SECT and used as reference of human dose. From this reason, we calculated the relationship between CTDI and human dose for SECT and DECT and compared between those two relationships. CT-AEC is the technique aiming at dose reduction and image quality optimization. CT-AEC is divided into the angular (x-y axis) and longitudinal (z-axis) tube current modulation (TCM). In order to incorporate CT-AEC into the simulation for accurate CT dose evaluation, we calculated TCM data. In this study, all simulations were performed using the Electron Gamma Shower ver.5 (EGS5) which is one of the Monte Carlo simulation codes.

## Materials and Methods

### 1. Accuracy validation of dose evaluation for DECT

Fig.1 shows simulation geometry for DECT. The geometric condition of a non-helical x-ray CT unit TCT-300 (Toshiba Medical Systems, Tochigi, JAPAN) was used. X-ray tube voltages were 80kV, 140kV (for DECT) and 120kV (for SECT). Three incident energy spectra were calculated using Tucker's formula [1]. In DECT, dose allocation between 80kV and 140kV was calculated by simulation to equalize the photon number of 80kV and 140kV reaching detector. As a result, the dose allocation was 80kV:140kV=69.4%:30.6%. Furthermore, we investigated the effect of varying the dose allocation from 80kV:140kV=59.4%:40.6% to 79.4%:20.6% at intervals of 5%. Two cylindrical phantoms (16 cm in diameter and 15 cm thick) were used. One of these phantoms was made from polymethylmethacrylate (PMMA). PMMA phantom is equivalent to the phantom for CTDI measurement. Another phantom was made from water. We assumed that water phantom is equivalent to human body. To calculate the relationship between CTDI and human dose, the absorbed dose ratio ( $R_{ad}$ ) was defined as

$$R_{ad} = \frac{D_w}{D_p}$$

where  $D_w$  was absorbed dose in water phantom.  $D_p$  was absorbed dose in PMMA phantom.  $R_{ad}$  was calculated at five (center and four peripheral) positions for SECT and DECT, respectively. Human dose can be estimated by multiplying CTDI by  $R_{ad}$ .

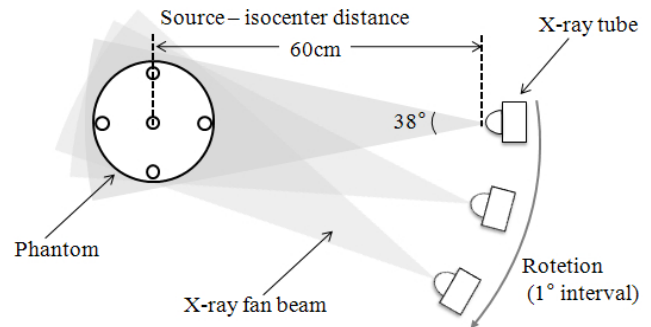


Fig.1 Simulation geometry for DECT

### 2. Calculating longitudinal (z-axis) TCM data

Fig.2 shows simulation geometry for longitudinal (z-axis) TCM. The geometric condition of multi-slice CT unit Aquilion64 (Toshiba Medical Systems, Tochigi, JAPAN) was used. X-ray tube voltages were 120kV calculated using Tucker's formula [1] and x-ray beam which had width equal to the phantom and thickness of 1cm was used. CTU-41 (Kyoto Kagaku, Kyoto, Japan) voxel phantom was used in this simulation. The voxel phantom is made by assigning each material (soft tissue, bone, lung and air) into each voxel read from DICOM images taken by CT. This makes it possible to simulate anthropomorphic phantom which has complicated structure. In this study, we calculated the longitudinal (z-axis) TCM data. X-ray tube was moved in steps of 1.0cm along z axis direction and the number of photons reaching CT detectors was counted. Then the number of incident photons at each slice was calculated to equalize the photon number reaching detector. Longitudinal (z-axis) TCM data which equalize the image standard deviation (SD) of each slice was obtained. The calculated data was compared with the TCM data represented on CTU-41 image made by Aquilion64.

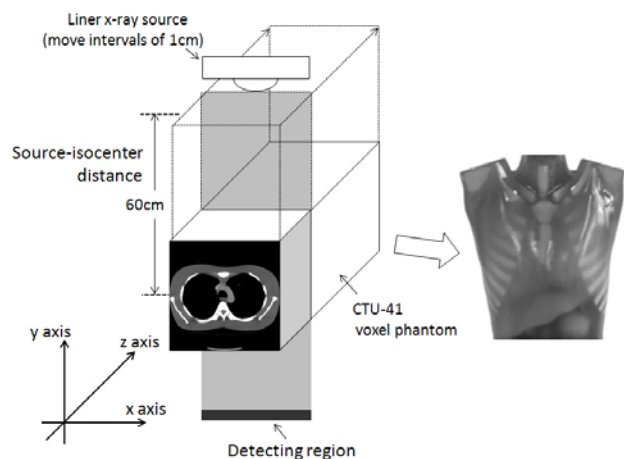


Fig.2 Simulation geometry for longitudinal (z-axis) TCM

## Results and discussion

### 1. Accuracy validation of dose evaluation for DECT

Fig.3 shows  $R_{ad}$  of SECT and DECT at each dose allocation in the center position of phantom. The  $R_{ad}$  of SECT (=1.414) was higher than that of DECT (=1.351). As the dose of 80kV increased,  $R_{ad}$  of DECT decreased from 1.362 to 1.331. If the human dose was estimated from  $R_{ad}$  of SECT, the human dose in DECT was overestimated by 4.5%. In the peripheral position, averages of  $R_{ad}$  for both CT were about the same ( $R_{ad}$  of SECT=1.367  $R_{ad}$  of DECT=1.371). As the dose of 80kV increased,  $R_{ad}$  increased slightly from 1.356 to 1.377. In order to discuss the reason of these results, absorbed dose in the center position of the phantom for a variety of tube voltage was simulated. Tube voltage was increased from 80kV to 140kV at intervals of 10kV. The spectrum for each tube voltage was calculated using Tucker's formula [1]. For more detailed discussion, the absorption dose was divided primary x-ray component and scattering x-ray component. The changes of absorbed dose for a variety of tube voltage in the water phantom are shown in fig.4 (a) and in the PMMA phantom are shown in fig.4 (b). In the both phantoms, total absorbed dose was increased with increasing the tube voltage and the scattering x-ray component contributed largely to the increase in absorbed dose. But the increasing range of the total absorption dose differed between water phantom and PMMA phantom. In the water phantom, the total absorbed dose varied from 3.29 (100%) to 4.74 (144%). As for the PMMA phantom, the total absorbed dose varied from 2.46 (100%) to 3.30 (134%). Thus, the changes of  $R_{ad}$  in Fig.3 were caused by difference of the increasing range of absorbed dose between water and PMMA phantom with increase in the tube voltage.

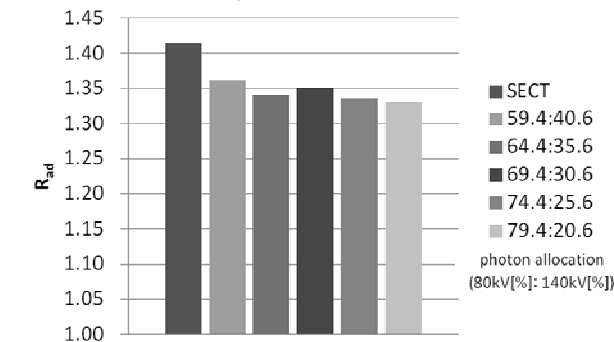


Fig.3 Changes of  $R_{ad}$  by a variance of dose allocation at center position in the cylindrical phantom

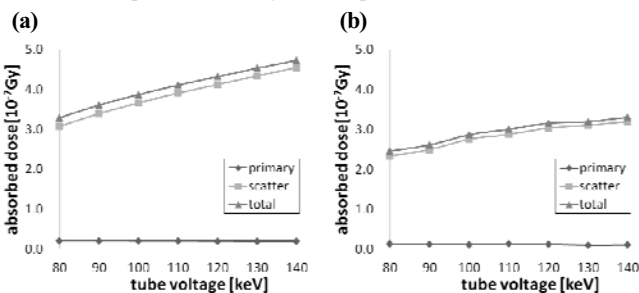


Fig.4 Changes of absorbed dose caused by variation of tube voltage (a) Water phantom. (b) PMMA phantom.

### 2. Calculating longitudinal (z-axis) TCM data

Fig.5 shows the longitudinal (z-axis) TCM data of CTU-41 phantom represented on Aquilion64 console (represented data) and calculated using simulation. To perform the longitudinal (z-axis) TCM equalizing the image SD of each slice, the value of TCM data is applied to the mAs value at each slice. The form of two data was more or less the same. The simulation data was, however lower than the represented data at slices from first to fifth (neck), slices from eighth to seventeenth (from apex of lung to aortic root) and slices from twenty-fourth to thirty-first (from left ventricle to apex pulmonis). Therefore, it is necessary to make these differences small.

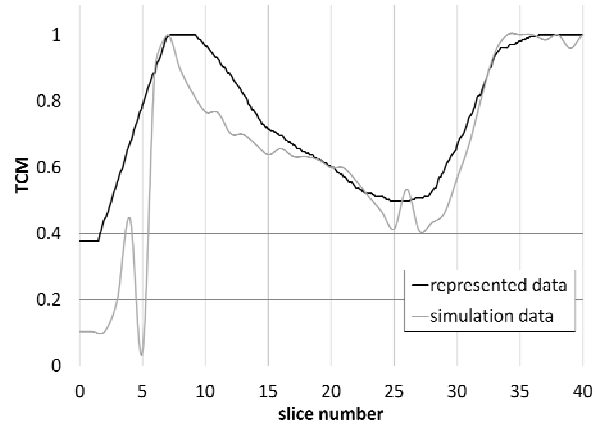


Fig.5 Longitudinal (z-axis) TCM data (represented and simulation)

### Conclusions

In accuracy validation of dose evaluation for DECT, we calculated the relationship between CTDI and human dose for SE CT and DECT and compared between the two relationships. As a result, the relationship of DECT was slightly different to the one of SECT. This study shows that human dose in DECT was overestimated by 4.5% if human dose was estimated from SECT's relationship between CTDI and human dose. In calculating tube longitudinal (z-axis) TCM data, the form of represented and simulation data was more or less the same. Further studies are needed to make the differences small. Furthermore, we hope to calculate angular (x-y axis) TCM data and to compare with measured data for simulating more accurate CT-AEC.

### References

- [1] Douglas M. Tucker, Gary T. Barnes and Dev P. Chakraborty, Semiempirical model for generating tungsten target x-ray spectra, Med. Phys. 18, 211-218 (1991)
- [2] Lifeng Yu, Andrew N. Primak, Xin Liu, and Cynthia H. McCollough, Image quality optimization and evaluation of linearly mixed images in dual-source, dual-energy CT, Med. Phys. 36, 1019-1024 (2009)
- [3] McCollough C.H., Bruesewitz M.R., Kofler J.M. Jr., CT Dose Reduction and Dose Management Tools: Overview of Available Options, Radiographics, Mar-Apr; 26(2):503-12 (2006)

### Author address

E-Mail: [hayashi.daiki@g.mbox.nagoya-u.ac.jp](mailto:hayashi.daiki@g.mbox.nagoya-u.ac.jp)



# ESTIMATION OF DOSE DISTRIBUTION IN CTDI PHANTOM IN CBCT USING MONTE CARLO SIMULATION

Tomonobu Haba<sup>1)</sup>, Shuji Koyama<sup>1)</sup>

1) Department of Radiological Sciences, Nagoya University Graduate School of Medicine, Nagoya, Japan

## Introduction

Recently, 320 detector row cone beam CT (CBCT) has been used in clinical examination. In 320 detector row CBCT, dose distribution in phantom is complicated because its wide x-ray beamwidth of 160 mm causes more scattering component of x-ray. The understanding of detailed dose distribution in phantom is useful for dose estimation in CT scanner. However, the measurement of dose distribution in phantom for kilovoltage x-ray beams is difficult because there are problems related to large gradients in the dose distribution and the large energy dependence of most dosimetry systems [1]. In this study, we calculated dose distribution in CT dose index (CTDI) phantom in 320 detector row CBCT using Monte Carlo (MC) simulation.

## Materials and Methods

### 1. Conformity of MC simulation with measurement

It is important to checking the conformity of MC simulation with measurement. We calculated and measured  $CTDI_{100}$  in a non-helical x-ray CT unit TCT-300 (Toshiba Medical Systems, Tochigi, Japan).  $CTDI_{100}$  is CTDI measured using 100 mm long CT chamber. The x-ray tube voltage was 120 kV, and source center distance (SCD) was 600 mm. PMMA cylindrical phantom of 300 mm diameter and 150 mm length and CT ionization chamber (CT chamber) of 100 mm length were used. In the phantom, there were five cylindrical cavities in different depth along the cylinder axis to insert the CT chamber; the depths were 11, 59, 81, 115, and 150 mm from the phantom surface. **Fig.1** shows measurement geometry. The phantom was supported using wooden blocks and the bed was removed from scan area. This is because it is difficult to incorporate the effect of x-ray scattering and attenuation of CT patient bed in the simulation.

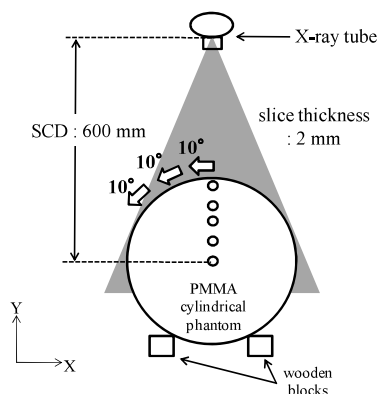


**Fig.1** measurement geometry

In addition, it is also difficult to incorporate the effect of x-ray tube rotation overlapping in the simulation because the overlapping angle has not been disclosed. Therefore, a scanogram mode (non-rotating mode) was used. The phantom was rotated by 10 degrees up to full circle in a counterclockwise direction and each dose was integrated by using CT chamber.

In MC simulation, the simulation geometry was the same as the above measurement geometry. Energy spectrums as x-ray source along the fan beam of the CT were generated by Tucker's formula [2] based on AL HVL measured on each angle. The effect of the beam shaping filter was incorporated into the simulation.

### 2. PDD calculated by MC simulation in CBCT

Percentage depth dose (PDD) along depth direction from surface to surface through the center point in 320 detector row CBCT was calculated using MC simulation. This CBCT geometry was applied to previous TCT-300 geometry, but the beamwidth was changed from 2 mm to 160 mm. **Fig.2** shows CBCT geometry in MC simulation. The x-y coordinate plane is parallel to the transverse axis, and the z coordinate axis (z axis) is parallel to the longitudinal axis of cylindrical phantom. The x coordinate axis (x axis) is horizontal to the floor, and the y coordinate axis (y axis) is perpendicular to the floor. Phantom was PMMA cylinder of 320 mm diameter and 600 mm length. In this condition, one rotating scan was performed. PDD was calculated per 1.0 mm depth. The size of calculation region was 10.0 mm (x), 1.0 mm (y), and 100 mm or 300 mm (z). The size of z direction was on the assumption of 100 mm long or 300 mm long CT chamber. Energy deposition by primary x-ray and Compton scatter x-ray was accounted for separately.

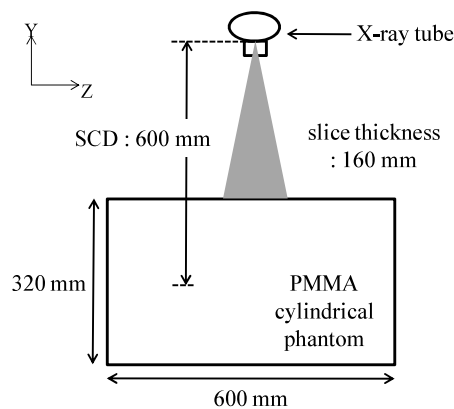


**Fig.2** MC simulation geometry in CBCT

## Results

### 1. Conformity of MC simulation with measurement

**Table 1** shows the conformity of MC simulation with measurement. The depth showed the distance from the phantom surface to the center of CT chamber. Each depth dose was normalized to 11 mm depth dose in the MC simulation and the measurement. Percent Average Error (PAE) is given as follows:

$$PAE = \frac{D_m - D_s}{D_m} \times 100 \text{ [%]}$$

where  $D_m$  was the normalized measured dose,  $D_s$  was the normalized calculated dose. In the **Table 1**, PAE was within  $\pm 2.4 \%$  in all depth.

**Table 1** the conformity of simulation with measurement

depth from the phantom surface [mm]	normalized dose		PAE [%]
	simulation ( $D_s$ )	measurement ( $D_m$ )	
11	1.0	1.0	0.0
59	0.94	0.93	-1.5
81	0.84	0.85	2.2
115	0.77	0.77	-0.3
150	0.71	0.73	2.4

### 2. PDD calculated by MC simulation in CBCT

**Fig.3** and **4** show PDDs which were calculated on the assumption of 100 mm long and 300 mm long CT chamber, respectively. Continuous line indicated total deposition energy (primary or Compton scatter); broken line indicated deposition energy which only came from Compton scattering component of x-ray; and dotted line indicated deposition energy which came from primary component of x-ray. The depth indicated the distance from the upper surface to the lower surface of the phantom. Each of deposition energies was normalized to the total deposition energy in the surface region. In **Fig.3**, peak dose of total deposit energy was 11.0 % higher than phantom surface dose. The position of maximum dose was 18.0 mm depth from the phantom surface. In **Fig.4**, peak dose of total deposit energy was 22.0 % higher than phantom surface dose. The position of maximum dose was 30.0 mm depth from the phantom surface.

## Discussion

In **Table 1**, there is a good agreement between MC simulation and measurement because PAE is within  $\pm 2.4 \%$  in all depth.

In **Fig.3** and **4**, detail analysis of energy deposition finds that Compton scattering is contributed largely to maximum dose position shifting. This effect is greater with the 300 mm long CT chamber than with the 100 mm long CT chamber. This is because the 300 mm length along the direction of z axis covers wide x-ray beamwidth in 320 detector row CBCT and is more deposited Compton scatter component of x-rays. Our results showed that, in the existing CTDI estimation of CBCT, peripheral measurement position of 10 mm depth was different to maximum dose position. We considered that this effect is very important for CTDI estimation. Dose estimation in CT scanner is now performing using  $CTDI_{100}$ . In 320 detector row CBCT, however, Geleijns et al. said that  $CTDI_{100}$  underestimated  $CTDI_{300}$  [3]. In this research, we also thought that it is better to measure CTDI using 300mm CT chamber because maximum dose position shifting is remarkable.

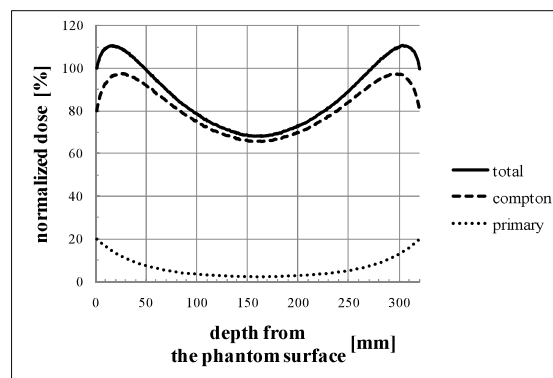


**Fig.3** PDD which was calculated on the assumption of 100 mm CT chamber

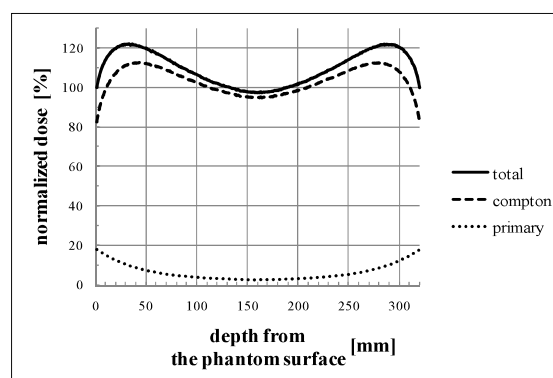


**Fig.4** PDD which was calculated on the assumption of 300 mm CT chamber

The measurement using 300 mm long CT chamber is, however, impractical in clinical quality assurance since it is difficult to develop long chamber which has uniform sensitivity and to handle the large and heavy PMMA phantom. Along with the popularization of 320 detector row CBCT, dosimetry of x-ray CT will become even more complex.

## Conclusion

In this research, we calculated PDD using MC simulation in order to analyze the dose distribution in the CTDI phantom in 320 detector row CBCT. We thought that it is also important to consider about the measurement depth of peripheral positions in CTDI phantom in 320 detector row CBCT.

## References

- [1] C L Fletcher, J A Mills, An assessment of GafChromic film for measuring 50 kV and 100 kV percentage depth dose curves, *Phys.Med.Biol.* 53 (2008) N209-N218.
- [2] Douglas M. Tucker, Semiempirical model for generating tungsten target x-ray spectra, *Med. Phys.* 18 (1991)
- [3] J Geleijns, M S Artells, P W de Bruin, R Matter, Y Muramatsu, M F McNitt-Gray, Computed tomography dose assessment for a 160 mm wide, 320 detector row, cone beam CT scanner, *Phys.Med.Biol.* 10 (2009) 3141-3159.

## Author address

E-Mail: [haba.tomonobu@f.mbox.nagoya-u.ac.jp](mailto:haba.tomonobu@f.mbox.nagoya-u.ac.jp)

# SIGNAL-TO-NOISE RATIOS CONSIDERED AS HUMAN VISUAL CHARACTERISTICS

Yui Hayashi<sup>1)</sup>, Yuki Yoshi Kimura<sup>1)</sup>, Maki Yamada<sup>1)</sup>, Naotoshi Fujita<sup>2)</sup>, Akiko Horii<sup>1)</sup>, Yoshie Kodera<sup>1)</sup>

- 1) Department of Radiological Sciences, Nagoya University Graduate School of Medicine, Nagoya, Japan  
2) Department of Radiological Technology, Nagoya University Hospital, Nagoya, Japan

## Introduction

The effects of various imaging parameters on detectability have not yet been clarified, and image quality indices do not necessarily equate with visual image quality. Therefore, in this study, we investigated the usefulness of signal-to-noise ratios (SNRs) considered as human visual characteristics, such as the visual spatial frequency response and the internal noise that serves as an additional noise component in the eye-brain system of a human observer.

## Materials and Methods

*Equipment used in this study:* The Mermaid MGU-100B mammogram, REGIUS V stage Model 190 computed radiography (CR) reader, and CP1M200 (with columnar crystal phosphors) CR plate were used in this study. All this equipment was manufactured by Konica Minolta MG. For perceptual evaluation, we used a 5-megapixel liquid crystal display (5-MP LCD; Totoku). To measure Wiener spectrum (WS), a single-lens reflex type digital camera, Nikon D70.

*Study.1:* Examination by the 16AFC procedure using simulated images.

We calculated three types of SNRs corresponding to the amplitude model (SNRa), matched filter model (SNRm), and internal noise model (SNRi). SNRa is calculated from the amplitude of the signal and the standard deviation of the noise. This is not considered human visual characteristics and the size of the signal. SNRm is defined as

$$SNR_m^2 = 2\pi \int_0^\infty u \frac{S_s^2(u)}{S_w(u)} du.$$

$S_s(u)$  and  $S_w(u)$  denote the displayed signal spectrum and the overall WS respectively.  $S_s$  is the product of the spatial frequency characteristics of the signal, the overall modulation transfer function (MTF). For the WS calculation, we displayed the image on a 5-MP LCD and captured it using a digital camera. We calculated the WS by the two-dimensional fast Fourier transform (2D-FFT) method. SNRm depends only upon the physical characteristics of the image, and thus, it can be used as the physical image quality index of the model. SNRi, which takes into consideration the spatial frequency response of the human visual system and the internal noise of the eye-brain system, is given as

$$SNR_i = \frac{S_p}{\sqrt{N_p^2 + N_i^2}}$$

$$S_p = \left[ 2\pi \int_0^\infty u S_s^2(u) VRF^2(u) du \right]^{\frac{1}{2}}$$

$$N_p = \left[ \frac{2\pi \int_0^\infty u S_s^2(u) S_w(u) VRF^4(u) du}{2\pi \int_0^\infty u S_s^2(u) VRF^2(u) du} \right]^{\frac{1}{2}}.$$

$VRF(u)$  is the visual spatial frequency response of the human observer. The value of VRF was obtained from previous literature.  $N_i$  denotes the internal noise caused by the noise

inherent in the observer, for instance, the noise associated with neurophysiological instability and memory fluctuations of the observer. The internal noise was estimated to be 0.0076 in brightness contrast units.

In this perceptual evaluation, we employed a 16-alternative forced choice (16-AFC) procedure for the observer performance experiments. In such a procedure, the observer is asked to choose one of 16 boxes as the signal location in a test image. The test images were simulated by the superimposition of low-contrast signals on a uniform noisy background. This involved 15 imaging cases with various signal sizes, signal contrasts, exposure levels, and number of acrylic plates used as breast phantoms. (Table 1) We displayed the test images on a 5-MP LCD and examined the detection performance. The observation distance was 30 cm and observation time was less than 5 s per image. Six observers participated in this experiment. The signal detection rate was defined as the number of detected signals divided by the total number of images. We studied the relationship between SNR and the signal detection rate using Spearman's rank correlation coefficient.

Table 1. Summary of imaging cases.

The exposure parameter		Thickness of acrylic plates[cm]	Diameter [number of pixels]	Contrast of brightness
[kV]	[mAs]			
28	50	6	30	1.84
28	50	6	30	3.61
28	50	6	30	4.48
28	50	6	30	5.33
28	50	6	30	6.98
28	50	6	30	8.58
28	50	6	40	4.48
28	50	6	40	8.58
28	16	6	30	8.58
28	32	6	30	8.58
28	50	4	30	5.33
28	50	4	30	8.58
28	50	8	30	8.58
28	50	8	30	10.87
24	50	6	30	8.58

*Study.2:* Examination of reduced image using mammography phantom.

We obtained the image of the mammography phantom using Phase Contrast Mammography (PCM) system. The

mammography phantom is the CIRS Model 011A breast phantom (Fig.1). The exposure condition was 28kV, 50mAs, and target/filter is Mo/Mo. Because the matrix size of the PCM image is very large, we reduced the PCM image by some interpolating methods and reduction ratios. Interpolating methods were nearest neighbor (NN), bilinear (BL), and bicubic (BC). The reduction rate was 5 cases from 0.169 to 0.571. In the same way as first examination, we obtained the spatial frequency characteristics of the mass, the overall MTF, and the overall WS. We calculated three types of SNRs corresponding to SNRa, SNRm, and SNRi. In this perceptual evaluation, the observer read masses in the mammography phantom images and scored. For example, 1 point is that the mass looked completely round shape. Zero point is that the observer could not see the mass. We displayed the phantom images on a 5-MP LCD and examined the detection performance. The observation distance was 30 cm and observation time was optional. Ten radiation technologists participated in this experiment. We studied the relationship between SNR and the average score of ten observers.

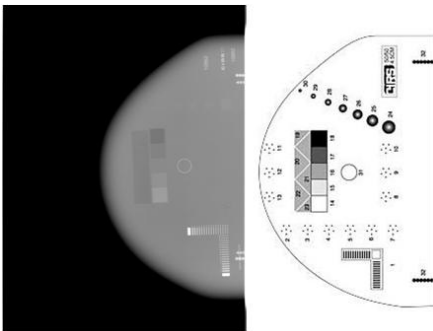


Fig.1. CIRS Model 011A breast phantom

**Results**

Spearman’s rank correlation coefficients of Study1 and Study2 are shown in Table 2. The relationships between the average scores and the three SNR types (Study 2) are shown in Fig.2.

Table 2. Spearman’s rank correlation coefficients

Perceptual evaluation vs. image quality index of:	Correlation coefficient	
	Study1	Study2
Amplitude model	0.45	0.26
Matched filter model	0.90	0.80
Internal noise model	0.93	0.79

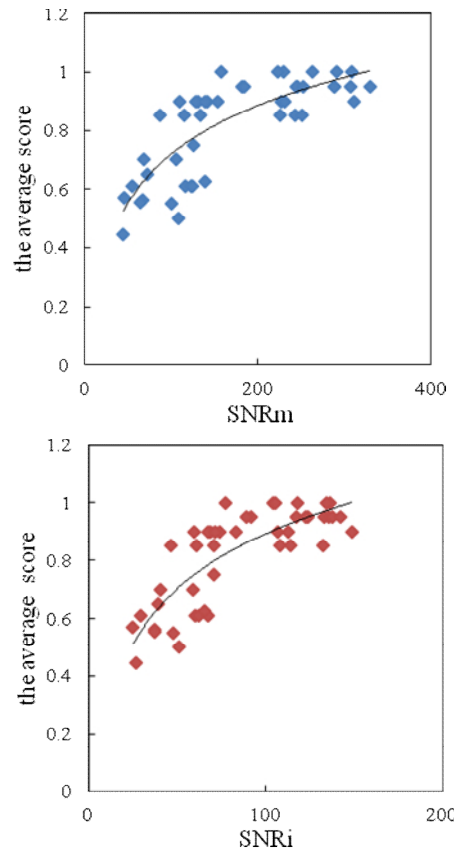
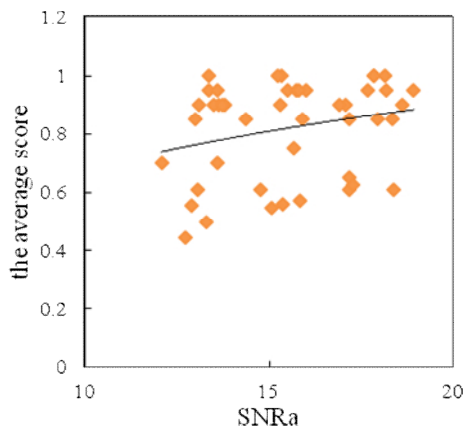


Fig.2. Relationship between the average scores and the three SNR types.

**Discussion**

The correlation coefficient of the SNRa was 0.45 and 0.26. There is poor correlation between the SNRa and the detectability. Because The SNRa depends only upon the signal contrast and the standard deviation of the noise, and the size of the signal is not taken into account. So we think SNRa is inadequate image evaluation. We confirmed that the correlation coefficient of SNRi was the highest among the three SNR types. The SNRm is not considered human visual characteristics, but it was at the same level as the SNRi.

In the previous study, SNR was calculated using film density of screen-film system. However we used brightness of the display in digital mammography systems. We thought that brightness is better to compare SNR with the perceptual evaluation.

**Conclusions**

SNRm and SNRi explained the visual image quality well. Therefore, we conclude that SNRm and SNRi are useful for evaluating low-contrast images.

**References**

[1] Loo, L.-N. D., Doi, K. and Metz, C. E., “A comparison of physical image quality indices and observer performance in the radiographic detection of nylon beads,” *Phys. Med. Biol.* 29(7), 837-856 (1984).  
 [2] Jain, A. K., [Fundamentals of Digital Image Processing], Prentice-Hall Inc., Upper Saddle River, 569 pp(1989).  
 [3] Ishida, M., Doi, K., Loo, L. N., Metz, C. E. and Lehr, J. L., “Digital image processing: effect on detectability of simulated low-contrast radiographic patterns,” *Radiology* 150, 569-575 (1984).

**Author address**

E-Mail: hayashi.yui@b.mbox.nagoya-u.ac.jp

## **Development of a high resolution gamma camera system with photon counting semiconductor detector : a simulation study**

Young-Jin Lee, Hyun-Ju Ryu, Hyo-Min Cho, Seung-Wan Lee, Yu-Na Choi, Hee-Joung Kim.  
Department of Radiological Science, College of Health Sciences,  
Yonsei University, Gangwon-do, Republic of Korea

**INTRODUCTION:** The photon counting detector based on CdTe or CZT has some benefits compare to the scintillation detector. Especially, the signal from photons was collected individually for each pixel, and thus the intrinsic resolution of the detector is almost the same as the size of a pixel. However a disadvantage of this detector was a loss in sensitivity due to the small pixel on the detector. By using the pixelated parallel-hole collimator, we may be able to improve the sensitivity and the spatial resolution. In this study, we simulated the gamma camera system using the photon counting detector based on CdTe and CZT, and evaluated the performance of these systems.

The purpose of this paper was to evaluate high resolution gamma camera system with semiconductor detector, which had very small pixels, using pixelated parallel-hole collimator. For that purpose, we evaluated the sensitivity, spatial resolution and contrast resolution with Geant4 Application for Tomographic Emission (GATE) simulation.

**METHODS:** To evaluate the image performance of our proposed system we performed simulation with GATE version 6 in this study. The proposed system used the CZT and CdTe detector with small pixel. The size of pixel was  $0.35 \times 0.35 \text{ mm}^2$  and the number of pixels was  $128 \times 128$  such as PID 350 (Ajat Oy Ltd., Finland) CdTe detector. The thickness of the detector was 1 mm. We designed pixelated parallel-hole collimator, which has the same hole size to the pixel size. The shape of the collimator hole was square, and the size of the hole was  $0.3 \times 0.3 \text{ mm}^2$ . The thickness of the septum was  $0.05 \times 0.05 \text{ mm}^2$  and length of a hole was 20 mm. We evaluated the sensitivity, spatial resolution, and contrast resolution to identify the pixelated parallel-hole collimator that provides the best resolution and highest sensitivity of the gamma camera system based on a PID 350 CdTe detector.

**RESULTS:** The average measurement data of the sensitivity was 0.00464 counts/sec/kBq. Also, the proposed system achieved 0.42 mm spatial resolution when the source was located 0 cm from the collimator. The acquired spatial resolution was similar to spatial resolution of the pinhole collimator, which was the best in the field of nuclear medicine. The results showed that the measured average data of CZT detector and CdTe detector was 96.30% and 96.72%, respectively.

**CONCLUSION:** We simulated a high resolution gamma camera system with a CdTe and CZT detector and pixelated parallel-hole collimator. By using the pixelated parallel-hole collimator, we were able to acquire the excellent spatial resolution since the intrinsic resolution was equal to the pixel size. Also the results of simulations showed that gamma camera images measured with a CdTe and CZT detector had high contrast resolution and superb sensitivity in small pixel condition. In conclusion, our results demonstrated that we established the high resolution gamma camera system with the pixelated parallel-hole collimator.

# Optimal Design of a Deblurring Filter in Digital Tomosynthesis for the Application of Dental X-ray Imaging

J. E. Oh<sup>1),2)</sup>, H. S. Cho<sup>1)</sup>, D. S. Kim<sup>1)</sup>, S. I. Choi<sup>1),2)</sup>, Y. O. Park<sup>1)</sup>, D. K. Hong<sup>1),2)</sup>, U. K. Je<sup>1),2)</sup>,  
M. S. Lee<sup>1)</sup>, H. J. Kim<sup>1)</sup>, S. H. Lee<sup>1)</sup>, Y. S. Koo<sup>1),2)</sup>, and S. O. Na<sup>2)</sup>

1) Department of Radiological Science, Yonsei University, Wonju 220-710, Korea

2) R&D Center, Vatech Co. Ltd., Hwasung 445-811, Korea

**INTRODUCTION:** The application of digital tomosynthesis (DTS) in dental X-ray imaging such as endodontics or implant placement seems promising since it provides attractive advantages of low patient dose and less motion blur. Since DTS only provides incomplete 3D data of the imaged object(Fig.1), it is critical to design and incorporate an optimal deblurring filter into reconstruction algorithm.

**METHODS:** In this paper, we describe a systematic approach to optimal filter design(fig.2) and investigate the optimization of the scan process such as the scan angle, the number of projections, the object magnification, and so on, for optimal image quality. Tomosynthetic images are reconstructed by filtered backprojection (FBP) method as well as by simple backprojection method. In order to verify the usefulness of the DTS reconstruction algorithm, we developed a simulation code implemented in MATLAB 7.8® for systematic simulation studies, and also performed experimental works.

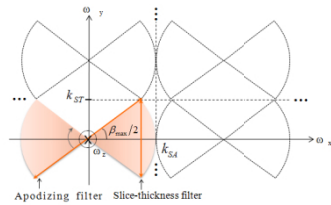


Fig. 1

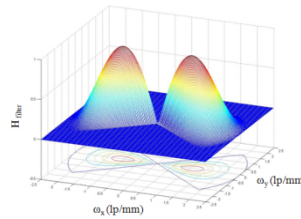


Fig. 2

**RESULTS:** In the simulation, DTS images were reconstructed for several simulation conditions ( $\beta_{max} = 35^\circ \sim 180^\circ$ ,  $\Delta\beta = 0.46^\circ \sim 3.0^\circ$ ) and the performance was evaluated by means of the ASF and the SDNR. As shown in Fig. 3, the ASF, as a measure of deblurring effect, may be sensitive to total scan angle, but not to scan angle step. It also seems to moderately sensitive to voxel size. We applied the same algorithm to our dental cone-beam CTs which have pixel sizes of 48  $\mu\text{m}$  and 200  $\mu\text{m}$ , and achieved very promising results with test conditions of  $\beta_{max} = 74^\circ$ ,  $\Delta\beta = 0.74^\circ$ . The blurring was mostly removed by the optimal deblurring filter we designed in Fig. 4.

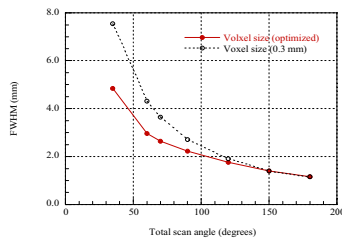


Fig. 3

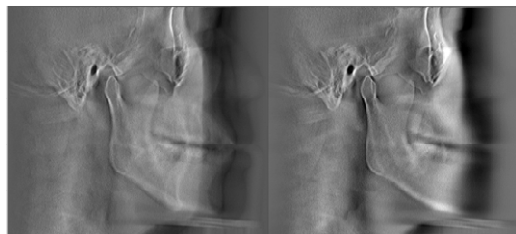


Fig. 4

**CONCLUSION:** According to our results, the blurring due to the incomplete sampling was mostly removed by the optimal deblurring filter we designed, thus recovering high spatial resolution as well as high contrast. We expect that the proposed reconstructed algorithm may be useful for our ongoing application of three-dimensional (3D) dental panoramic tomography.

## **Evaluation of Spectral Distortion Effects on X-ray Imaging with a Photon-Counting Detector**

Hyo-Min Cho, Yu-Na Choi, Seung-Wan Lee, Hyun-Ju Ryu, Young-Jin Lee, and Hee-Joung Kim

Department of Radiological Science, College of Health Sciences,  
Yonsei University, Gangwon-do, Republic of Korea

**INTRODUCTION:** The photon counting detector has received considerable interest in recent years due to its advantages over charge-integrating detectors. However, there are several factors that can limit to the use of the photon-counting detector. These include the charge sharing effects can't be controlled by operator and the pulse pile-up effects can be reduced by modulating incident number of photons. In this paper, we evaluated the effects of spectral distortion by pulse pile-up effect on X-ray imaging using simulation and experimentation.

**METHODS:** The photon-counting imaging system used in this study consisted of a micro focus X-ray source (L8601-01, Hamamatsu, Japan) and CdTe detector (PID 350, AJAT, Finland). The CdTe detector was positioned 1000 mm from the X-ray source focal spot. Phantom images and relevant energy spectra were acquired at 70 kVp and 10  $\mu$ A for 20 sec. The photon rejecter can decrease spectral distortion due to pulse pile-up by reducing amount of incident photon. Aluminum plate was used as photon rejecter. The X-ray tube output was filtered with three different aluminum plate thicknesses (1, 5, and 10 mm). The photon counting X-ray imaging system was simulated using the Geant4 Application for Tomographic Emission (GATE) V6. The detected image and spectrum were assumed to be ideal, without spectrum distortion. The contrast-to-noise ratio (CNR) between the material and background was considered as a comparison factor of spectral distortion effect on the image.

**RESULTS:** From the simulation study, the total number of photons was dramatically reduced according to aluminum filter thickness, especially at low energy. By contrast, the spectra showed high number of photons detected in the low energy part in experiment. Pulse pile-up effects that have not been completely corrected with 1 mm aluminum filter contribute to the more counts recorded at energies above 70 keV. Even though 5 and 10 mm aluminum filter minimized pulse pile-up effect the photon rejecter has the limited ability to reduce the pile-up effect. In addition, the photon rejecter separated electrical noise from the spectrum by reducing the number of photons. In the simulation results, the factor that contributed to the low CNR values with the thick aluminum filter was due to quantum noise by a lack of photons. In the experimental results, the effect of noise due to a lack of photons was very slight in comparison to the simulation results because the photon-counting detector was already limited an acceptable number of photons by detector electronics. However, the images were greatly influenced by the electronic noise which is distinguishable by filter thickness.

**CONCLUSION:** In conclusion, the spectral distortion affects the image quality by increasing low energy photons, but optimal photon rejecter is feasible to increase image quality by minimizing the pulse pile-up effect and remove separated electronic noise from the signal.

## **Development of a CdTe detector SPECT-CT system for a small animal imaging: a simulation study**

Hyun-Ju Ryu, Young-Jin Lee, Seung-Wan Lee, Hyo-Min Cho, Yu-Na Choi, Hee-Joung Kim  
Department of Radiological Science and Research Institute of Health Science, Yonsei  
University, Korea

**INTRODUCTION:** Single photon emission computed tomography (SPECT) system with a co-registered x-ray computed tomography (CT) image allows the fusion of functional information and morphologic information. In this study, a pinhole collimator SPECT system sharing a CdTe detector with a CT was designed. Geant4 application for tomographic emission (GATE) version 6 was used for the design simulation. Sensitivity and spatial resolution were measured to evaluate the system characteristics on an ideal condition.

**METHODS:** The SPECT/CT sharing a single CdTe detector was designed to have one gantry for both x-ray CT and SPECT system. The size of the detector was  $44.8 \times 44.8 \text{ mm}^2$  with  $128 \times 128$  pixels, and the thickness of the detector was 1 mm. The SPECT/CT system was designed with a pinhole collimator and CdTe detector (Oy Ajat Ltd., Finland) using GATE version 6.0. For the SPECT system, a pinhole collimator was designed to have a high spatial resolution. 60 projections were obtained for tomographic image acquisition of the SPECT system. The reconstruction was performed using ordered subset expectation maximization (OS-EM) algorithms. The x-ray generator was designed to rotate around the center of field of view (CFOV), and the gantry was rotated with x-ray tube and detector to have 256 projections of the object over 360 degree. The pinhole collimator was removed while the x-ray imaging was processed. For the CT imaging, 256 projections were acquired on 80 kVp with 50 mm aluminum filter to reduce low energy photon flux. A water phantom with background activity of 25 MBq and hot lesions with 100 MBq was simulated on both CT and SPECT system. Total 256 projections of CT images and 60 projections of SPECT images were reconstructed using OSEM algorithm. The energy window of the CT data acquisition was set from 30 keV to 80 keV.

**RESULTS:** The pinhole collimator was designed to have a sub-mm resolution for a small animal imaging SPECT system. Though the SPECT system was simulated in an ideal condition, the spatial resolution of the system was measured 0.48 mm as expected from the pinhole collimator geometry. The MTF curve was calculated from the PSF of the reconstructed point source image. The sensitivity of the system measured 0.354 cps/kBq from a Tc-99m point source. The phantom images of x-ray CT, SPECT were fused to demonstrate the image registration of different modalities.

**CONCLUSION:** The CdTe detector can be used for x-ray and gamma ray imaging system. The detector can be performed for both CT and SPECT system because of this characteristic. The object stays in a same position, and it gives an advantage on the image registration of different modalities. The designed pinhole collimator for single detector SPECT/CT had a fine spatial resolution for a small animal SPECT imaging. A CdTe detector with 1 mm thickness was evaluated in this study. The system will have better detection efficiency with a thicker CdTe detector. The designed pinhole collimator SPECT/CT with CdTe detector can be applied for the pre-clinical imaging system.



## Simulation study of in-beam PET system for dose verification in carbon ion therapy

Su jung An, Cheol-Ha Baek and Yong Hyun Chung.  
Department of Radiological Science, College of Health Sciences,  
Yonsei University, Gangwon-do, Republic of Korea

**INTRODUCTION:** Application of hadron such as carbon ion is being developed for cancer treatment. This is due to eligibility of charged particles in delivering most of their energy near the end of their range, called Bragg peak. However, accurate verification of dose delivery is required since the mis-alignment of the hadron beam can cause serious damage to normal tissues. PET scanner can be utilized to track the carbon beam down to the tumor by imaging the trail of the hadron-induced positron emitters in the irradiated volume. In this study, we designed and evaluated through Monte Carlo simulation the in-beam PET scanner for monitoring patient dose in carbon beam therapy.

### **METHODS:**

#### **2.1. Designing of in-beam PET scanner**

PET scanner with 30.2 cm inner diameter was designed for brain imaging. Each detector module consists of an LYSO array of  $13 \times 13$  elements with pixel size of  $4 \times 4 \times 30 \text{ mm}^3$  and four round PMTs with 25.4 mm diameter.

A C-shaped PET and a partial-ring PET were designed to avoid interference between PET detectors and the therapeutic carbon beam delivery and their performance were compared with a full-ring PET scanner. The C-shaped, partial-ring and full-ring scanners consist of 14, 12 and 16 detector modules, respectively,

To evaluate three types of PET, we simulated five point sources at different positions and measured spatial resolution and sensitivity.

#### **2.2. Generation of positron-emitting nuclei by carbon ions**

GATE (Version 6.1) was used to simulate the generation of positron emitting radio-nuclides by carbon irradiation in PMMA phantom. The beam profiles in the transverse directions were assumed to be a Gaussian with a FWHM of 10 mm. The beam energy spread was taken with a FWHM of 0.2%. To validate the simulator, yields of positron-emitting nuclei ( $^{11}\text{C}$ ,  $^{10}\text{C}$ , and  $^{15}\text{O}$ ) produced by 212.12, 259.5, 343.46 AMeV carbon in the PMMA phantom with  $9 \times 9 \times 30 \text{ cm}^3$  were compared to simulated and measured data from other groups. The yields of  $^{11}\text{C}$ ,  $^{10}\text{C}$ ,  $^{15}\text{O}$  produced by 170, 290, and 350 AMeV carbon beams (those energies were selected to be used in KHIMA) in the PMMA cylinder phantom with 20 cm diameter and 20 cm height were simulated. This output was used as an input file in subsequent PET image acquisition simulations.

#### **2.3. In-beam PET imaging with three types of PET scanners**

To calculate the number of positron annihilations used as source activity in PET imaging, ion beam was assumed that has a tunable time structure given by repetition of particle extractions (spills) and pause. PET images are acquired during half life of  $^{11}\text{C}$  nuclei on the assumption that carbon beam intensity was  $1 \times 10^8 \text{ \#/sec}$  and total therapeutic time of 2 minutes (48 seconds of irradiation). Phantom images were acquired for three types of scanners. Dose distribution was compared  $\beta^+$  activity distribution and PET image profile, respectively.

## Result:

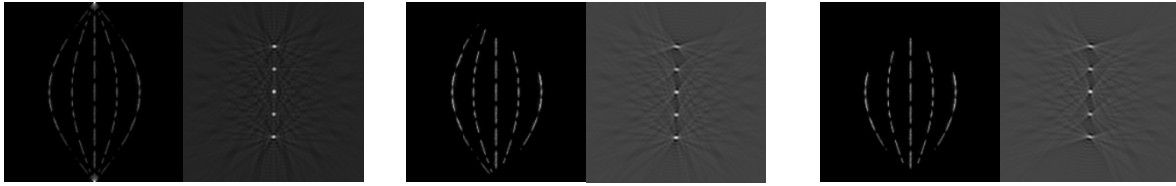


Fig. 1. The sinograms and reconstruction images of point sources at different positions obtained by three types of scanner by GATE simulation.

Fig 1 demonstrates simulated sinograms and reconstructed images of point sources at different positions acquired by three types of scanners. Spatial resolution in x- and y-directions and sensitivity are summarized in Table 1, 2 and 3. Results demonstrate that the spatial resolution in x-direction is reduced for sources located at periphery of FOV where detector modules are removed for carbon beam line. Sensitivity depends on the number of detector modules.

Detector type	X-axis Resolution [mm]				
	1	2	3	4	5
Full ring	7.93	6.23	5.88	6.36	7.70
C-type	9.29	7.15	7.33	8.63	14.59
Partial-ring	15.51	8.47	7.41	8.65	14.64

Table 1. X-axis Resolution of 5 points.

Detector type	Y-axis Resolution [mm]				
	1	2	3	4	5
Full ring	4.89	5.15	5.28	4.97	4.98
C-type	4.90	5.17	5.30	4.93	4.97
Partial-ring	4.88	5.13	5.32	4.94	4.98

Table 2. Y-axis Resolution of 5 points.

Detector type	Sensitivity (%)
Full ring	1.69
C-type	1.26
Partial-ring	1.12

Table 3. Sensitivity in 3 types of scanners.

Table 4 shows calculated yields of positron-emitting nuclei produced by 212.12, 259.5, and 343.46 AMeV of  $^{12}\text{C}$  ions to verify GATE simulator and results agree well with reference data. (per beam particle, in %) MCHIT is Simulated data and Experiment is measured data from [Phys. Med. Bio. 51 (2006) 6099-6112]. Table 5 summarized the calculated yields of positron-emitting nuclei produced by 170, 290, and 350 AMeV of  $^{12}\text{C}$  ions in the PMMA phantom. (per beam particle, in %)

	212.12 AMeV			259.5 AMeV			343.46 AMeV			170 AMeV	290 AMeV	350 AMeV
	MCHIT	Experiment	GATE6	MCHIT	Experiment	GATE6	MCHIT	Experiment	GATE6			
$^{11}\text{C}$	11.9	10.5±1.3	9.73	16.83	14.7±1.6	13.11	25.25	19.9±2.4	18.43	6.86	15.06	18.80
$^{10}\text{C}$	1.97	0.8±0.3	1.38	2.79	1.2±0.3	1.85	4.27	1.5±0.3	2.57	0.99	2.08	2.62
$^{15}\text{O}$	2.38	2.1±0.3	1.71	3.69	3.1±0.4	2.36	6.09	5.0±0.4	3.48	1.17	2.79	3.57

Table 4. Calculated yields of positron-emitting nuclei(per beam particle, in %) produced by 212.12, 259.5 and 343.46 AMeV  $^{12}\text{C}$  ions in the PMMA phantom.

Table 5. Calculated yields of positron-emitting nuclei(per beam particle, in %) produced by 170, 290, and 350 AMeV  $^{12}\text{C}$  ions in the PMMA phantom.

Reconstructed PET images and their longitudinal profiles are shown in Fig 3. For comparison, simulated dose distribution and  $\beta^+$  activity distribution are also shown.

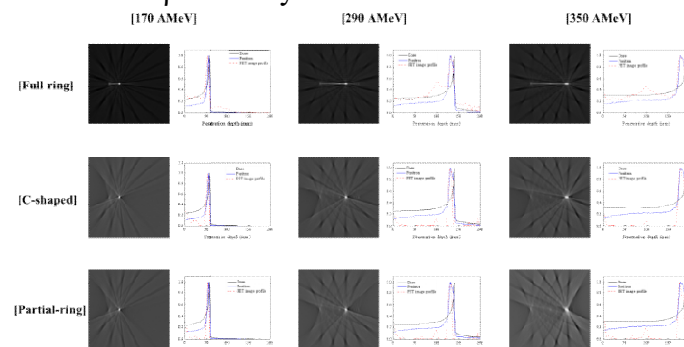


Fig. 3. Reconstructed PET images and their longitudinal profiles by three types of scanner by GATE simulation.

**CONCLUSION:** We proposed C-shaped and partial-ring scanners for dose verification in carbon ion therapy. We validated that GATE is feasible to predict the total yields of positron emitting nuclei with reasonable accuracy. The C-shaped scanner shows better spatial resolution and sensitivity than the partial-ring scanner. The accuracy of range estimation, especially for higher energy of carbon beam, is higher in the C-shaped scanner in comparison to partial-ring scanner due to their geometric difference. Though  $\beta^+$  activity distributions induced by carbon beams differ in shape from the corresponding dose distribution, there exists a decisive correlation between them, which can be used for the dose and range monitoring. Because the PET image profile is well matched with  $\beta^+$  activity distributions, we can conclude that PET has the potential feasibility for dose verification. Our investigation indicated that C-shaped scanner is more suitable as the in-beam PET.